IJMMM International Journal of
Minerals, Metallurgy and Materials
矿物冶金与材料学报（英文版）

High thermal conductivity and high strength magnesium alloy for high pressure die casting ultrathin-walled components

Jian Rong, Wenlong Xiao, Xinqing Zhao, Chaoli Ma, Haimiao Liao, Donglei He, Ming Chen, Meng Huang, and Chen Huang

Cite this article as:
Jian Rong, Wenlong Xiao, Xinqing Zhao, Chaoli Ma, Haimiao Liao, Donglei He, Ming Chen, Meng Huang, and Chen Huang, High thermal conductivity and high strength magnesium alloy for high pressure die casting ultrathin-walled components, *Int. J. Miner. Metall. Mater.*, 29(2022), No. 1, pp. 88-96. https://doi.org/10.1007/s12613-021-2318-y

View the article online at SpringerLink or IJMMM Webpage.

Articles you may be interested in

Z. M. Sheggaf, R. Ahmad, M. B. A. Asmael, and A. M. M. Elaswad, Solidification, microstructure, and mechanical properties of the as-cast ZRE1 magnesium alloy with different praseodymium contents, *Int. J. Miner. Metall. Mater.*, 24(2017), No. 11, pp. 1306-1320. https://doi.org/10.1007/s12613-017-1523-1

Chong Lin, Shu-sen Wu, Shu-lin Lü, Ping An, and He-bao Wu, Effects of high-pressure rheo-squeeze casting on the Fe-rich phases and mechanical properties of Al-17Si-(1,1.5)Fe alloys, *Int. J. Miner. Metall. Mater.*, 25(2018), No. 9, pp. 1018-1026. https://doi.org/10.1007/s12613-018-1652-1

A. V. Koltygin, V. E. Bazhenov, R. S. Khasenova, A. A. Komissarov, A. I. Bazlov, and V. A. Bautin, Effects of small additions of Zn on the microstructure, mechanical properties and corrosion resistance of WE43B Mg alloys, *Int. J. Miner. Metall. Mater.*, 26(2019), No. 7, pp. 858-868. https://doi.org/10.1007/s12613-019-1801-1

Yi-li Dai, Sheng-fu Yu, An-guo Huang, and Yu-sheng Shi, Microstructure and mechanical properties of high-strength low alloy steel by wire and arc additive manufacturing, *Int. J. Miner. Metall. Mater.*, 27(2020), No. 7, pp. 933-942. https://doi.org/10.1007/s12613-019-1919-1

Zhi-yong Xue, Yue-juan Ren, Wen-bo Luo, Yu Ren, Ping Xu, and Chao Xu, Microstructure evolution and mechanical properties of a large-sized ingot of Mg-9Gd-3Y-1.5Zn-0.5Zr (wt%) alloy after a lower-temperature homogenization treatment, *Int. J. Miner. Metall. Mater.*, 24(2017), No. 3, pp. 271-279. https://doi.org/10.1007/s12613-017-1405-6

Xing-hai Yang, Xiao-hua Chen, Shi-wei Pan, Zi-dong Wang, Kai-xuan Chen, Da-yong Li, and Jun-wei Qin, Microstructure and mechanical properties of ultralow carbon high-strength steel weld metals with or without Cu–Nb addition, *Int. J. Miner. Metall. Mater.*, 28(2021), No. 1, pp. 120-130. https://doi.org/10.1007/s12613-020-2159-0

IJMMM WeChat

QQ author group

International Journal of Minerals, Metallurgy and Materials
Volume 29, Number 1, January 2022, Page 88
https://doi.org/10.1007/s12613-021-2318-y

High thermal conductivity and high strength magnesium alloy for high pressure die casting ultrathin-walled components

*Jian Rong*1), *Wenlong Xiao*1),✉, *Xinqing Zhao*1), *Chaoli Ma*1), *Haimiao Liao*2), *Donglei He*1), *Ming Chen*2), *Meng Huang*3), *and Chen Huang*2)

1) Key Laboratory of Aerospace Advanced Materials and Performance of Ministry of Education, School of Materials Science and Engineering, Beihang University, Beijing 100191, China
2) Dongguan Qingniao Metal Material Co., Ltd., Dongguan 523000, China
3) Structural Technology Department, Hardware Technology Center, OPPO Guangdong Mobile Communications Co., Ltd., Dongguan 523000, China

(Received: 13 May 2021; revised: 10 June 2021; accepted: 17 June 2021)

Abstract: With the rapid development of 3C industries, the demand for high-thermal-conductivity magnesium alloys with high mechanical performance is increasing quickly. However, the thermal conductivities of most common Mg foundry alloys (such as Mg–9wt%–1wt%Zn) are still relatively low. In this study, we developed a high-thermal-conductivity Mg–4Al–4Zn–4RE–1Ca (wt%, AZEX4441) alloy with good mechanical properties for ultrathin-walled cellphone components via high-pressure die casting (HPDC). The HPDC AZEX4441 alloy exhibited a fine homogeneous microstructure (average grain size of 2.8 μm) with granular $Al_{11}RE_3$, fibrous Al_2REZn_2, and networked $Ca_6Mg_2Zn_3$ phases distributed at the grain boundaries. The room-temperature thermal conductivity of the HPDC AZEX4441 alloy was 94.4 W·m^{-1}·K^{-1}, which was much higher than 53.7 W·m^{-1}·K^{-1} of the HPDC AZ91D alloy. Al and Zn in the AZEX4441 alloy were largely consumed by the formation of $Al_{11}RE_3$, Al_2REZn_2, and $Ca_2Mg_6Zn_3$ phases because of the addition of RE and Ca. Therefore, the lattice distortion induced by solute atoms of the AZEX4441 alloy (0.171%) was much lower than that of the AZ91D alloy (0.441%), which was responsible for the high thermal conductivity of the AZEX4441 alloy. The AZEX4441 alloy exhibited a high yield strength of ~185 MPa, an ultimate tensile strength of ~233 MPa, and an elongation of ~4.2%. This result indicated that the tensile properties were comparable with those of the AZ91D alloy. Therefore, this study contributed to the development of high-performance Mg alloys with a combination of high thermal conductivity, high strength, and good castability.

Keywords: magnesium alloys; microstructure; thermal conductivity; mechanical properties; high-pressure die casting

1. Introduction

Magnesium (Mg) and its alloys have been widely explored in the fields of computer, communication, and consumer (3C) electronic products, automotive, and aerospace fields because of their low density, high specific strength, and good electromagnetic shielding [1–3]. With a high integration level in 3C products, the heat dissipation of materials can significantly influence the normal operation of components as a result of high heat density and operating temperature [4]. The requirement for materials with a combination of high heat dissipation capability and high strength is increasing rapidly. Pure Mg exhibits a high thermal conductivity of 156 W·m^{-1}·K^{-1}, which is next to lightweight pure Al (237 W·m^{-1}·K^{-1}) [5]. In addition, the heat capacity of Mg is lower than that of Al, and the heat dissipation effects of the former are better than those of Al; thus, Mg is a potential heat dissipation material [6–7]. However, the strength of pure Mg is relatively low and insufficient to meet the practical requirements of electronic components. The addition of alloying elements is an effective approach to enhance the mechanical properties of pure Mg, but it detrimentally influences the thermal conductivity of Mg as a result of elements being dissolved in the Mg matrix [8–10].

Previous studies have mainly focused on the effects of solute atoms, heat treatments, and deformations on the thermal conductivities of Mg alloys. Heat treatment significantly influences the thermal conductivities of Mg alloys. For example, the room-temperature thermal conductivity of Mg–Al–Mn and Mg–Zn–RE alloys subjected to a solution treatment is lower than that of the as-cast alloys because of increase in the concentrations of solute atoms [11–12]. Yuan *et al.* [9] studied the thermal characteristics of the as-cast and heat-treated (T6) Mg–Zn–Mn alloys and found that T6 aging treatment enhances thermal conductivity because of the decreased content of dissolved Zn through precipitation. Furthermore, hot plastic deformation can simultaneously improve the strength and heat dissipation of Mg alloys. Liu

---

✉ Corresponding author: Wenlong Xiao E-mail: wlxiao@buaa.edu.cn

et al. [13] reported that a Mg–2Mn–2.5La (wt%) alloy processed through hot extrusion exhibits high tensile properties and high thermal conductivity, i.e., it has an ultimate tensile strength (UTS) of 367 MPa, a yield strength (YS) of 359 MPa, and a thermal conductivity of 135 $W \cdot m^{-1} \cdot K^{-1}$. Solute atoms inevitably impair the thermal conductivity of Mg alloys by inducing lattice distortion, which can cause free electron scattering and phonon movement, while; conversely, the adverse influence of second phases on thermal conductivity is much weaker than that of solute atoms [13–14]. Hence, adding appropriate alloying elements is a promising method to form second-phase particles other than solute atoms and consequently produce Mg alloys with superior thermal conductivity and high strength.

As for industrial application, most Mg alloys in the 3C industry are processed via high-pressure die casting (HPDC) because of its high production rates and relatively low cost [15–16]. To our knowledge, some of the commonly used HPDC Mg alloys are Mg–Al-based alloys, such as Mg–6Al–0.5Mn (AM60, wt%) and Mg–9Al–1Zn (AZ91D, wt%), because of their excellent castability and mechanical properties [17–18]. Nevertheless, the thermal conductivities of these alloys are relatively low, thereby limiting the broad application of Mg alloys. For instance, the AZ91D alloy, which has been widely used in the important components of portable laptops and cellphones, shows high strength, superior die castability, and excellent corrosion resistance [19]. However, the room-temperature thermal conductivity of an as-cast AZ91D alloy is 51.2 $W \cdot m^{-1} \cdot K^{-1}$[20]. Although a high Al content in Mg alloys can improve their strength and die castability, massive Al addition inevitably results in a significant decrease in thermal conductivity because of a high amount of dissolved Al in the Mg matrix. Rudajevová *et al.* [11] studied the effect of Al on the thermal conductivity of Mg–Al–Mn alloys and revealed that thermal conductivity decreases significantly as the content of Al solute atoms increases. Pan *et al.* [4] measured the thermal conductivities of Mg–Al, Mg–Zn, Mg–Sn, Mg–Zr, Mg–Mn, and Mg–Ca alloys. They found that the adverse effect of solute elements on thermal conductivity can be arranged in the following sequence: Zn < Al < Ca < Sn < Mn < Zr. This result indicates that Zn shows the weakest influence on decreasing thermal conductivity among other elements. Therefore, reducing the Al content and increasing the Zn content seem suitable for high-thermal-conductivity Mg alloys. However, if the amount of the added Al in Mg–Al alloys is less than 4wt%, the die castability may be decreased.

The die castability of Mg alloys can be improved by increasing the amount of added Zn up to 4wt%, whereas excessive amounts of Zn may lead to hot cracking and die sticking problems, especially those for HPDC ultrathin components [15,21]. As appropriate contents of Zn and Al are added, the addition of rare earths (REs) helps restrain low-melting-point eutectic phases by forming thermally stable $Al_{11}RE_3$ and Al_2REZn_2 phases, which can improve mechanical properties [22]. Furthermore, the formation of RE-containing intermetallic phases can decrease the content of solution elements by consuming Al and Zn atoms, which can enhance thermal conductivity [23]. A Mg–4Al–4Zn–4RE (wt%, ZAE444) alloy processed through HPDC has been developed, and it exhibits good die castability and mechanical properties comparable with those of AZ91D alloys; however, the ultrathin-walled products and thermal properties of this alloy have yet to be further explored [24]. The micro addition of Ca to Mg–Al–Zn–RE system alloys can further consume Zn solute elements by forming $Ca_2Mg_6Zn_3$ phases; as such, it helps improve thermal conductivity. Furthermore, Ca addition can promote grain refinement and enhance strength [25–26]. However, the high content of Ca addition (>0.1wt%) may cause sticking or hot tearing during casting [27–28]. Apart from Al, Zn, RE, and Ca, Mn (<0.3wt%) can play a role in micro addition to improve corrosion resistance effectively by decreasing the Fe content in Mg alloys [29].

In the present study, a Mg–4Al–4Zn–4RE–1Ca (AZEX 4441, in wt%, hereafter not mentioned) alloy was chosen as the base alloy to produce a novel high-thermal-conductivity and high-strength Mg–Al–Zn–RE–Ca alloy, which was suitable for HPDC ultrathin-walled cellphone components. Differences in microstructure, thermal conductivity, and tensile properties between the HPDC AZEX4441 and commercial HPDC AZ91D alloy were investigated. The microstructure–property relationship, especially the role of alloying elements in microstructures and properties, was discussed in detail.

2. Experimental

The AZ91 alloy was prepared from a commercially available AZ91D alloy, and the AZEX4441 alloy was prepared from commercially available pure Mg (99.90wt%), commercial pure Al (99.90wt%), pure Zn (99.90wt%), and Mg–30Ca and Mg–30RE (RE = Ce-rich mischmetal) master alloys. The original measured compositions of RE were 65.24Ce and 34.45La. These alloying components were completely melted in a stainless steel crucible by using an electric resistance furnace under the protection of a gas mixture of CO_2 and SF_6 at ~710°C. Before HPDC, the melt was held at ~680°C for 40 min and then cast into a steel mold preheated to ~220°C by using an IMPRESS 200T cold-chamber machine. This steel mold was used to produce magnesium cellphone components with a minimum wall thickness of 0.4 mm. The service conditions of the HPDC were as follows: ram velocity, 2.25 $m \cdot s^{-1}$; injection pressure, 40 MPa; die holding time, 5–7 s; and biscuit size, 40 mm. About 30–40 shots were made for each alloy. After HPDC, the real product images are presented in Fig. 1. The AZ91D and AZEX4441 alloys exhibited good die castability without hot cracking. The chemical compositions of the studied alloys achieved through an inductively coupled plasma–optical emission spectrometer are recorded in Table 1. The solidification behavior was analyzed through differential thermal analysis (DTA, SDT600, America) with a heating rate of 10°C·min^{-1}.

Phase constituents were identified through RINT-2000 X-ray diffraction (XRD) by using Cu K_α radiation at a voltage of 40 kV, a scanning angle from 20° to 80°, and a scanning

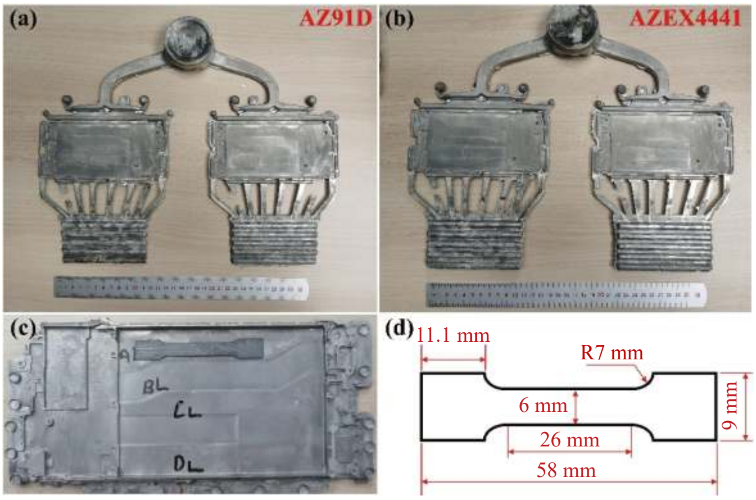

Fig. 1. Product images of HPDC AZ91D (a) and AZEX4441 alloys (b), and location (c) and size (d) of the tensile sample.

Table 1. Experimental compositions of the HPDC AZ91D and AZEX4441 alloys wt%

Alloy	Al	Zn	Ce	La	Ca	Mn	Mg
AZ91D	9.82	0.591	—	—	—	0.248	Bal.
AZEX4441	3.88	3.36	2.22	1.17	0.85	0.024	Bal.

speed of 4°·min^{-1}. The microstructures were characterized through JSM-7001F field emission scanning electron microscopy (SEM) and JEM-2100F transmission electron microscopy (TEM) equipped with an INCA-X-Max energy dispersive spectrometer (EDS). The metallographic samples for SEM were cut from the same position of each product, polished, and etched in nital (2 mL of nitric acid, and 23 mL of ethanol) for ~6 s. Thin foils for TEM were prepared by ion milling. The tensile specimens were cut from the same location (Fig. 1(c)). Their size is presented in Fig. 1(d). The room-temperature tensile tests were conducted using an Instron 8801 testing system at a strain rate of 3.0×10^{-3} s^{-1}.

The thermal conductivity (λ) of the studied alloys was calculated with the following equation:

$$\lambda = \alpha \cdot \rho \cdot C_\mathrm{p} \tag{1}$$

where α, ρ, and C_p are the thermal diffusivity (mm^2·s^{-1}), density (g·mm^{-3}), and specific heat capacity (J·g^{-1}·K^{-1})), respectively. The thermal diffusivity (α) was determined via the laser flash method by using a NETZSCH LFA 457 instrument. The HPDC samples were subjected to room-temperature density (ρ) measurements via the Archimedes method. Heat capacity (C_p) was measured using a NETZSCH 214 Nevio differential scanning calorimeter.

3. Results and discussions

3.1. Phase constitution

Fig. 2 shows the XRD analysis of the HPDC alloys. α-Mg and $Mg_{17}Al_{12}$ phases were detected in the HPDC AZ91D alloy (Fig. 2(a)), which was consistent with the results reported in the AZ91D alloy subjected to HPDC. In Fig. 2(b), the AZEX4441 alloy was composed of α-Mg, Al_2REZn_2, $Al_{11}RE_3$, and $Ca_6Mg_2Zn_3$ phases, whereas no $Mg_{17}Al_{12}$ and Mg–Al–Zn ternary phases were detected. The result was supposed to be similar to the previous study [30]. RE addition (3wt%–4wt%) in the Mg–Al–Zn alloys suppressed the formation of the low-melting-point $Mg_{17}Al_{12}$ phase by forming high-melting-point RE-containing intermetallic phases [22,31]. Furthermore, the main RE-containing phases are $Al_{11}RE_3$ and Al_2REZn_2 in the HPDC ZAE444 alloy [25]. As for the Mg–Al–Zn–RE–Ca system alloys, the addition of RE consumed Al and Zn to form RE-containing intermetallic phases during the initial solidification stage, and Ca addition promoted Ca-containing phases formed at the residual liquid solidification stage [30,32].

In general, solidification behavior determines mechanical

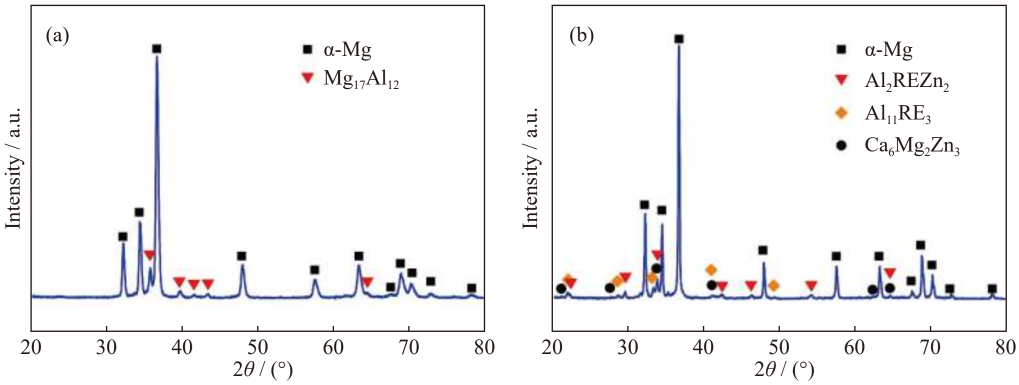

Fig. 2. XRD results of the HPDC alloys: (a) AZ91D; (b) AZEX4441.

performance, thermal properties, and die castability to a certain degree [33]. In Fig. 3, the DTA heating patterns of the HPDC AZ91D and AZEX4441 alloys were used to analyze solidification behavior, and each endothermic peak represented the dissolution of the labeled phase. The solidification behavior of the studied alloys could be determined on the basis of the XRD results and DTA curves. For the HPDC AZ91D alloy, the endothermic peaks related to the melting of α-Mg and $Mg_{17}Al_{12}$ phases were measured to be ~587°C and ~433°C, respectively. The endothermic peak of α-Mg for the AZEX4441 increased to ~610°C compared with that of the AZ91D alloy. In addition to α-Mg, two other endothermic peaks at ~589°C and ~501°C were supposed to be the phase transformation of RE-containing phases and $Ca_2Mg_6Zn_3$, respectively. Therefore, the formation of RE-containing phases (Al_2REZn_2 and $Al_{11}RE_3$) in the AZEX4441 alloy followed the formation of α-Mg at the initial stage of solidification. Subsequently, $Ca_6Mg_2Zn_3$ phase and RE-containing phases formed during the solidification stage of the residual liquid. were supposed to be the phase transformation of RE-containing phases and $Ca_2Mg_6Zn_3$, respectively. Therefore, the formation of RE-containing phases (Al_2REZn_2 and $Al_{11}RE_3$) in the AZEX4441 alloy followed the formation of α-Mg at the initial stage of solidification. Subsequently, $Ca_6Mg_2Zn_3$ phase and RE-containing phases formed during the solidification stage of the residual liquid.

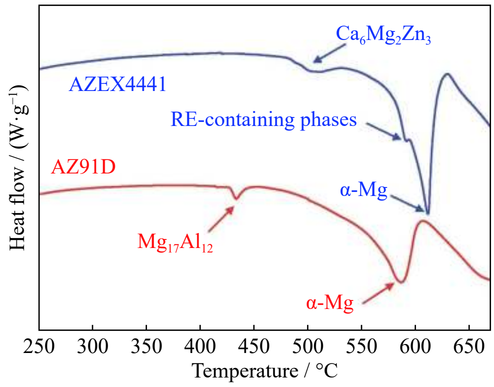

Fig. 3. DTA heating patterns of HPDC alloys.

3.2. Microstructural characterization

The typical back-scattered electron (BSE) images are presented in Fig. 4 to confirm the morphological characteristics and distribution of the second phases formed in the studied HPDC alloys. Fig. 4(a) and (b) reveals that the microstructure of the HPDC AZ91D alloy consisted of an α-Mg solid solution with an average grain size of ~4.2 μm and continuous networked β-$Mg_{17}Al_{12}$ eutectic phases distributed along the grain boundaries. In Fig. 4(c) and (d), the HPDC AZEX4441 alloy showed a fine homogeneous equiaxed grain structure with an average grain size of ~2.9 μm. Three typical morphologies (granular, fibrous, and networked) of intermetallic compounds concentrated at the grain boundaries were observed in the AZEX4441 alloy. The XRD result and the contrast demonstrated that the majority of intermetallic compounds showed that granular and fibrous structures with bright contrast likely belonged to RE-containing phases, and the networked structure with gray contrast corresponded to the $Ca_6Mg_2Zn_3$ phase. The morphological characteristics of RE-containing phases and $Ca_6Mg_2Zn_3$ phases are similar to the observation in the Mg–Al–Zn–RE–Ca alloys [30,32]. TEM analysis coupled with EDS was performed later to further identify the morphological characteristics and composition of intermetallic compounds.

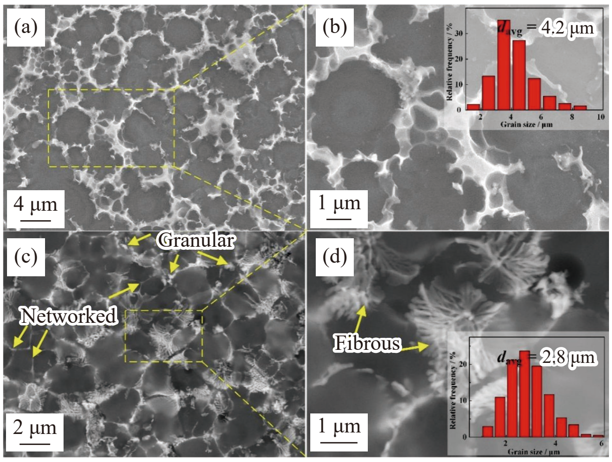

Fig. 4. BSE images of HPDC AZ91 alloy (a, b) and HPDC AZEX4441 alloy (c, d). Inset: grain size distribution images, d_{avg} strands for the average grain size.

The bright-field (BF) TEM image and the corresponding selected area electron diffraction (SAED) of HPDC AZ91 alloy are presented in Fig. 5. The networked $Mg_{17}Al_{12}$ eutectic phase, which was determined by the SAED patterns shown in Fig. 5(b) and (c), is illustrated in Fig. 5(a). The Al and Zn concentrations in α-Mg were measured to be 6.2wt% and 1.4wt%, respectively. Fig. 6 shows the BF-TEM images and the corresponding SAED patterns coupled with the EDS analysis of the HPDC AZEX4441 alloy. In Fig. 6(a)–(c), the AZEX4441 alloy consisted of granular, fibrous, and networked phases distributed at the grain boundaries, which were similar to the BSE observation (Fig. 4(c) and (d)). The types of the eutectic phases with different morphologies were further analyzed through SAED (Fig. 6(d)–(f)). The elemental compositions of each phase examined via EDS are listed in Fig. 6(g)–(i) and Table 2. The SAED pattern of the granular phase marked with A was indexed to an orthorhombic structure with measured lattice parameters of a = 0.4431 nm, b = 1.0132 nm, and c = 1.31424 nm, which were consistent with the $Al_{11}RE_3$ phase (Fig. 6(d)). The composition measured through EDS was $Mg_{32.9}Al_{41.5}Zn_{4.8}La_{5.2}Ce_{10.6}Ca_{5.0}$ (at%), indicating that certain amounts of Zn and Ca were dissolved in the $Al_{11}RE_3$ phase (Fig. 6(g)). The fibrous phase was large, and it belonged to a tetragonal structure with the space group I4/mmm (a = b = 0.425 nm, c = 1.102 nm) according to the SAED. This phase was validated to be Al_2REZn_2 (Fig. 6(e)). The EDS result shown in Fig. 6(h) indicated that this phase contained an average composition of $Mg_{22.8}Al_{38.6}Zn_{19.6}La_{4.8}Ce_{7.0}Ca_{7.2}$ (at%). The (Al or Zn)/RE atomic ratio signific-

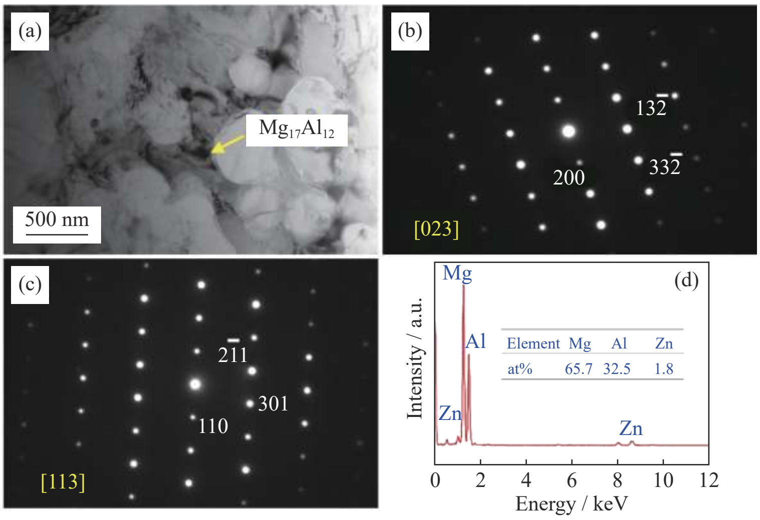

Fig. 5. Bright-field TEM images of HPDC AZ91 alloy (a) and SAED patterns from [023] (b) and [113] (c), and EDS spectrum (d) of $Mg_{17}Al_{12}$.

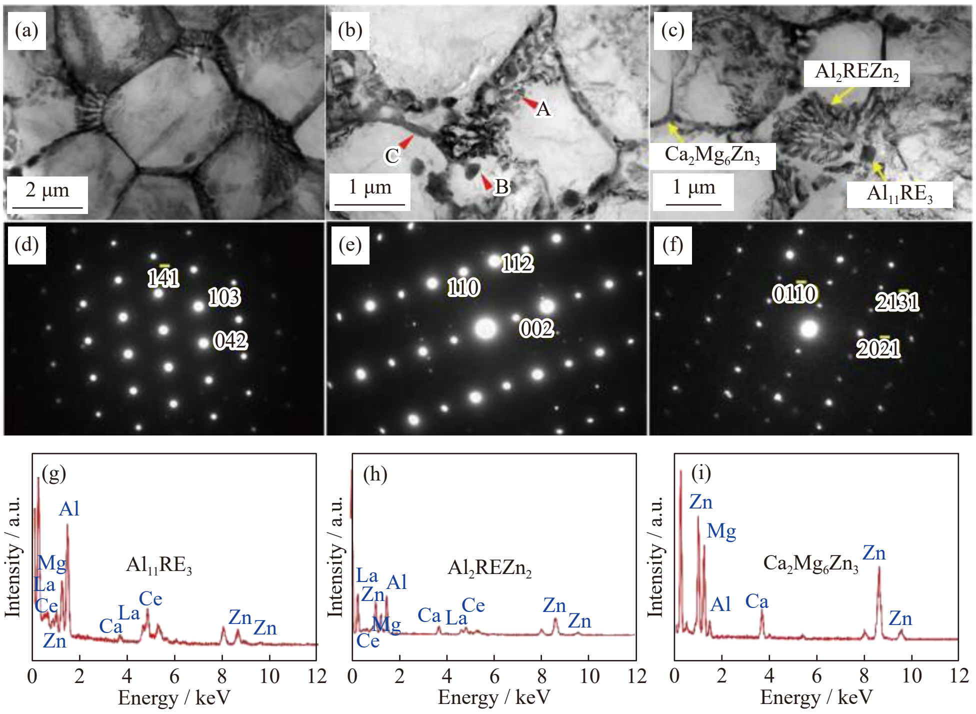

Fig. 6. (a–c) Bright-field TEM images of HPDC AZEX4441 alloy; (d–f) corresponding SAED patterns taken from the eutectic phase of A, B, and C in (b), respectively; (g–i) EDS spectra of the eutectic phases of A, B, and C in (b), respectively.

Table 2. EDS results (average atomic percentage) of the phases formed in HPDC AZEX4441 alloy at%

Phase	Al	Zn	La	Ce	Ca	Mg
Granular $Al_{11}RE_3$	41.5	4.8	5.2	10.6	5.0	32.9
Fibrous Al_2REZn_2	38.6	19.6	4.8	7.0	7.2	22.8
Networked $Ca_2Mg_6Zn_3$	11.57	25.53	—	—	13.24	49.66
α-Mg matrix	1.3	0.6	—	—	0.2	97.9

antly exceeded the expected stoichiometry of 2 probably because of the influence of the matrix, which is similar to the results reported in Mg–Zn–Al–La–Ca alloys [32]. The intensities of Zn and Ca in the networked eutectic phases were higher than those in the granular and fibrous phases, whereas no RE peaks were observed in the former (Fig. 6(i)). The EDS analysis and the SAED pattern shown in Fig. 6(f) confirmed that the networked phase was $Ca_2Mg_6Zn_3$.

3.3. Thermal conductivities

The room-temperature thermal properties of the AZEX4441 and AZ91D alloys subjected to HPDC are recorded in Table 3. The density and special heat capacity of the HPDC AZ91D and AZEX4441 alloys slightly differed.

Table 3. Thermal properties and lattice strain of the studied alloys at room temperature

Composition	Thermal diffusivity, α / ($mm^2 \cdot s^{-1}$)	Special heat capacity, C_p / ($J \cdot m^{-1} \cdot K^{-1}$)	Density, ρ / ($g \cdot cm^{-3}$)	Thermal conductivity, λ / ($W \cdot m^{-1} \cdot K^{-1}$)	Lattice strain / %
AZ91D	28.998±0.005	1.021±0.002	1.813±0.003	53.7±0.4	0.441±0.0027
AZEX4441	51.644±0.003	0.979±0.003	1.867±0.002	94.4±0.5	0.171±0.0015

However, the room-temperature thermal diffusivity of the AZEX4441 alloy was much higher than that of the AZ91D alloy. The thermal conductivities of the studied alloys were calculated from the thermal diffusivity, density, and specific heat capacity by using Eq. (1). Therefore, in this study, the thermal conductivity of the AZEX4441 alloy was higher than that of the AZ91D alloy, i.e., the thermal conductivities of the former and the latter were 94.4 and 53.7 $W \cdot m^{-1} \cdot K^{-1}$, respectively.

In general, solute atoms tend to reduce the thermal conductivity of Mg alloys because solute atoms can cause lattice distortion and thus limit the free movement and conductions of electrons and phonons [34–36]. Furthermore, a decrease in the thermal conductivities of Mg alloys caused by solute atoms is considered to be much larger than that by second phases because the lattice distortion caused by solute elements is much more serious than that by second phases [13–14]. In the present work, the AZ91D and AZEX4441 alloys had high contents of second phases (Fig. 4), but solute atoms (Al and Zn) of the AZEX4441 alloy were much lower than that of the AZ91D alloy. The lattice distortions (Table 3) calculated with Jade 9.0 by using the function of the size and strain plot were 0.171% and 0.441% for the HPDC AZEX4441 and AZ91D alloys, respectively. For the AZ91D alloy, the serious lattice distortion induced by a large amount of Al solute elements (6.2wt%) led to the reduction in the thermal conductivity of the AZ91D alloy. The contents of Al and Zn in the AZEX4441 alloy were largely consumed by the formation of $Al_{11}RE_3$, Al_2REZn_2, and $Ca_2Mg_6Zn_3$ phases compared with those of the AZ91D alloy because of the addition of RE and Ca. The lattice distortion induced by the solute atoms of the AZEX4441 alloy (0.171%) was much lower than that of the AZ91D alloy (0.441%), which was responsible for the higher thermal conductivity of the AZEX4441 alloy.

3.4. Mechanical properties

The typical tensile curves of HPDC AZ91D and AZEX4441 alloys are shown in Fig. 7. The average tensile properties are recorded in Table 4. The AZEX4441 alloy exhibited a YS of ~185 MPa, a UTS of ~233 MPa, and an elongation of ~4.2%; that is, the AZEX4441 alloy showed comparable YS, a slightly lower UTS, and a higher elongation than the AZ91D alloys, which had a YS of ~188 MPa, a UTS of ~255 MPa, and an elongation of ~3.0%. The YS of the thin-walled AZ91D specimen in the present study was much higher by ~30 MPa than the traditional HPDC AZ91D specimens. Grain refinement, solute atoms, and fine second phases are pivotal factors responsible for enhancing the YS of Mg alloys [24,37–38]. Hence, the YS (σ_y) of Mg alloys can be described as

$$\sigma_y = \sigma_{gb} + \sigma_{ss} + \sigma_{ds} \tag{2}$$

where σ_{gb} is the fine-grain strengthening, σ_{ss} is the solid solution strengthening, and σ_{ds} is the second-phase strengthening.

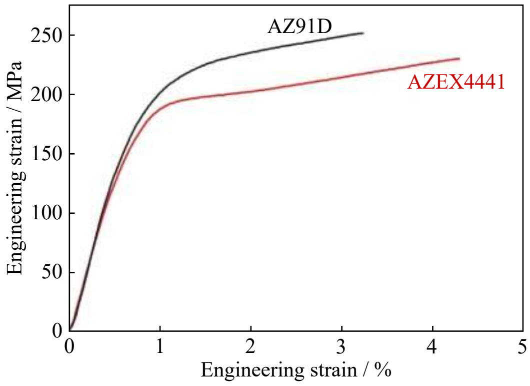

Fig. 7. Tensile engineering stress–strain curves of the studied alloys at room temperature.

Table 4. Tensile properties of the studied alloys at room temperature

Alloys	Yield strength, $\sigma_{0.2}$ / MPa	Tensile strength, σ_b / MPa	Elongation, ε / %
AZ91D	188±1	255±3	3.0±0.2
AZEX4441	185±4	233±3	4.2±0.2

The grain structure of the HPDC AZEX4441 alloy (d_{avg} = ~2.8 μm) was finer than that of the HPDC AZ91D alloy (d_{avg} = 4.2 μm) because of the addition of RE and Ca (Fig. 4). The increment in YS contributed by the fine-grain strengthening of the studied alloys was estimated by using the Hall–Petch equation:

$$\sigma_{gb} = kd^{-1/2} \tag{3}$$

where d and k are the average grain size and the coefficient (~0.26 $MPa \cdot m^{1/2}$ [37–40]), respectively. The strength contributions from the fine-grain structures of AZEX4441 and AZ91D alloy were 155 and 127 MPa, respectively. This result indicated that the fine-grain strengthening in the AZEX4441 alloy enhanced compared with that in the AZ91D alloy. Solid solution strengthening also plays a critical role in determining strength. For the AZ91D alloy, the α-Mg matrix contained a high content of Al, contributing to the strong solid solution strengthening. Nevertheless, the low content of solute atoms in the AZEX4441 alloy led to a significant reduction of solid solution strengthening compared with that in the AZ91D alloy. Apart from the above factors (grain size and solute atoms), second-phase strengthening related to the category, size, and morphological characteristics of the second phases occurred in the studied alloys [41]. REs and Ca additions enhance the strength of Mg–Al–Zn alloys through grain boundary reinforcement from RE- and Ca-containing phases [42–44]. Zhang *et al*. [32] investigated the variation in the tensile properties of Mg–Zn–Al-based alloys by adding La and Ca and found that the second-phase strengthening effect of the networked $Ca_2Mg_6Zn_3$ phase is better than that of large lamellar Al_2LaZn_2 phases at room temperature. Furthermore, Xiao *et al*. [24] evaluated the influence of Zn additions on the strength of the HPDC AE44 alloy and revealed that the replacement of Al–RE intermetallic compounds with coarse Al_2REZn_2 phases reduces second-phase strengthening because of increasing Zn additions. In the present study, the high volume fractions of fine granular $Al_{11}RE_3$ phases and networked $Ca_2Mg_6Zn_3$ phases distributed along the grain boundaries were the main strengthening phase in the AZEX4441 alloy because of the weak second-phase strengthening effect of large fibrous Al_2REZn_2 phases. The exclusive strengthening phases in the AZ91D alloy were large continuous networked $Mg_{17}Al_{12}$ eutectic phases. Thus, the grain boundary reinforcement of the AZEX4441 alloy was stronger than that of the AZ91D alloy because of the finer and more evenly distributed RE- and Ca-containing phases. Therefore, the high YS of the AZEX4441 alloy was mainly ascribed to the strong fine-grain strengthening because of the fine-grain structure and grain boundary reinforcement from RE- and Ca-containing intermetallic phases. The high YS of the AZ91D alloy was attributed to fine-grain strengthening and solid solution strengthening. Furthermore, the YS between AZEX4441 and AZ91D alloys might be similar because the strength contribution from the enhanced fine-grain strengthening, stronger grain boundary reinforcement, and weak solid solution strengthening in the AZEX4441 alloy was comparable with the strong solid solution strengthening, weak grain boundary reinforcement, and fine-grain strengthening in the AZ91D alloy.

The strain hardening capacity is considered one of the important factors in estimating the plastic deformation behavior of metals, influencing strength (UTS) and elongation. The Hollomon equation ($\sigma_{\rm ture} = K \cdot \epsilon_{\rm ture}^{n}$) is applied to evaluate the strain hardening capacity of the studied alloys, where n is the strain hardening exponent, and K is the strength coefficient [45]. In the present study, the HPDC AZ91D and AZEX4441 alloys had average n of 0.23 and 0.18, respectively, indicating that the strain hardening capacity of the former was higher than that of the latter. Therefore, the UTS of the AZ91 alloy was higher than that of the AZEX4441 alloy mainly because of the enhanced strain hardening capacity. Solute atoms can improve the strain hardening capacity by reducing the dynamic recovery rate of dislocations, thereby leading to a high dislocation density during plastic deformation [46]. The high content of solute atoms contributed to the strong strain hardening capacity of the AZ91D alloy. The elongation of the AZ91D alloy was lower than that of the AZEX4441 alloy, although n of the AZ91D alloy was higher (0.23). Fig. 8 shows the tensile fracture morphology of the HPDC AZ91D and AZEX4441 alloys. The fractograph of the AZ91D and AZEX4441 alloys exhibited typical intergranular fracture characteristics containing numerous clear ridges and smooth dissociation facets, which were consistent with the low ductility (3.0%–4.2%) of the HPDC alloys because of the presence of numerous pores. Furthermore, the ductile fracture characteristic with a few coarse dimples was observed in the AZEX4441 alloy, thereby accounting for the better elongation of the AZEX4441 alloy than that of the AZ91D alloy. This finding was attributed to the formation of the high volume fraction of coarse continuous networked $Mg_{17}Al_{12}$ eutectic phases (Fig. 4 (a) and (b)), which easily induce stress concentration and act as the source of microcracks, in the AZ91D alloy. Consequently, elongation decreases.

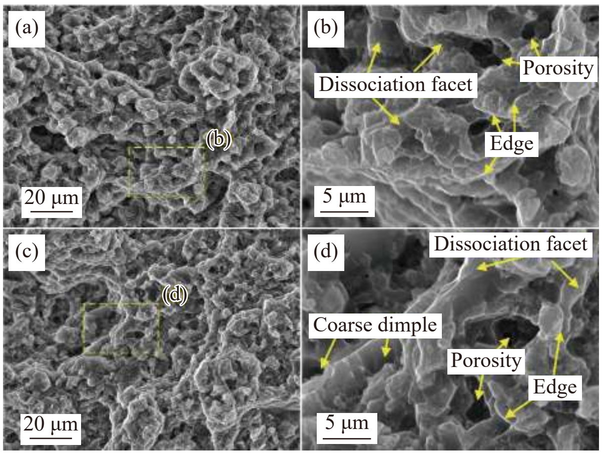

Fig. 8. SEM images of the tensile fracture: (a, b) AZ91D alloy; (c, d) AZEX4441 alloy.

4. Conclusions

In this work, the ultrathin wall cellphone components of AZEX4441 and AZ91D alloy were successfully prepared through HPDC. The microstructure and the resultant performance, including the tensile properties and thermal conductivities of these HPDC alloys, were comparatively investigated. This study might provide a basis for developing high-thermal-conductivity and high-strength HPDC Mg alloys. The following conclusions were obtained:

(1) The AZEX4441 alloy exhibited a fine homogeneous equiaxed grain structure ($d_{\rm avg}$ = ~2.8 μm) with granular $Al_{11}RE_3$, fibrous Al_2REZn_2, and networked $Ca_6Mg_2Zn_3$ intermetallic phases distributed at the grain boundaries. The second phase of the AZ91D alloy ($d_{\rm avg}$ = ~4.2 μm) was the coarse net-like $Mg_{17}Al_{12}$ eutectic phase.

(2) The room-temperature thermal conductivity of the AZEX4441 alloy was much higher than that of the AZ91D alloy, i.e., the thermal conductivity of the former was 94.4 $W \cdot m^{-1} \cdot K^{-1}$, whereas the latter was 53.7 $W \cdot m^{-1} \cdot K^{-1}$. The solute elements in the AZEX4441 alloy were largely consumed by forming RE- and Ca-containing intermetallic phases because of the addition of RE and Ca, which accounted for the significant increase in the thermal conductivity of the AZEX4441 alloy.

(3) The AZEX4441 alloy exhibited a comparable YS of

~185 MPa, a slightly lower UTS of ~233 MPa, and a higher elongation of ~4.2% than that of the AZ91D alloy. The high YS of the AZEX4441 alloy was mainly attributed to fine-grain strengthening from the fine-grain structure and grain boundary reinforcement from RE- and Ca-containing intermetallic phases.

Acknowledgements

The authors are grateful for the financial support by the National Key Research and Development Program of China (No. 2016YFB0301103) and the National Natural Science Foundation of China (NSFC, No. 51401010).

Conflict of Interest

The authors declare no potential conflict of interest.

References

[1] S.B. Li, X.Y. Yang, J.T. Hou, and W.B. Du, A review on thermal conductivity of magnesium and its alloys, *J. Magnesium Alloys*, 8(2020), No. 1, p. 78.

[2] J. Rong, P.Y. Wang, M. Zha, C. Wang, X.Y. Xu, H.Y. Wang, and Q.C. Jiang, Development of a novel strength ductile Mg–7Al–5Zn alloy with high superplasticity processed by hard-plate rolling (HPR), *J. Alloys Compd.*, 738(2018), p. 246.

[3] Y.Y. Zhou, P.H. Fu, L.M. Peng, D. Wang, Y.X. Wang, B. Hu, M. Liu, A.K. Sachdev, and W.J. Ding, Precipitation modification in cast Mg–1Nd–1Ce–Zr alloy by Zn addition, *J. Magnesium Alloys*, 7(2019), No. 1, p. 113.

[4] H.C. Pan, F.S. Pan, R.M. Yang, J. Peng, C.Y. Zhao, J. She, Z.Y. Gao, and A.T. Tang, Thermal and electrical conductivity of binary magnesium alloys, *J. Mater. Sci.*, 49(2014), No. 8, p. 3107.

[5] M.K. Kulekci, Magnesium and its alloys applications in automotive industry, *Int. J. Adv. Manuf. Technol.*, 39(2008), No. 9-10, p. 851.

[6] X.B. Li, W.T. Cao, and Y.Q. Bai, Study on the thermal dispersion of AZ91D, *J. Henan Polytech. Univ. Nat. Sci.*, 29(2010), No. 5, p. 685.

[7] W.X. Hu, Z.H. Yang, G.H. Chen, and Y.C. Cao, Research progress in influence of rare earth on microstructure and mechanical properties of magnesium alloy, *Chin. Rare Earths*, 35(2014), No. 5, p. 89.

[8] G.Q. Li, J.H. Zhang, R.Z. Wu, Y. Feng, S.J. Liu, X.J. Wang, Y.F. Jiao, Q. Yang, and J. Meng, Development of high mechanical properties and moderate thermal conductivity cast Mg alloy with multiple RE via heat treatment, *J. Mater. Sci. Technol.*, 34(2018), No. 7, p. 1076.

[9] J.W. Yuan, K. Zhang, X.H. Zhang, X.G. Li, T. Li, Y.J. Li, M.L. Ma, and G.L. Shi, Thermal characteristics of Mg–Zn–Mn alloys with high specific strength and high thermal conductivity, *J. Alloys Compd.*, 578(2013), p. 32.

[10] C.J. Chen, Q.D. Wang, and D.D. Yin, Thermal properties of Mg–11Y–5Gd–2Zn–0.5Zr (wt.%) alloy, *J. Alloys Compd.*, 487(2009), No. 1-2, p. 560.

[11] A. Rudajevová, M. Staněk, and P. Lukáč, Determination of thermal diffusivity and thermal conductivity of Mg–Al alloys, *Mater. Sci. Eng. A*, 341(2003), No. 1-2, p. 152.

[12] M. Yamasaki and Y. Kawamura, Thermal diffusivity and thermal conductivity of Mg–Zn-rare earth element alloys with long-period stacking ordered phase, *Scripta Mater.*, 60(2009), No. 4, p. 264.

[13] Y.F. Liu, X.G. Qiao, Z.T. Li, Z.H. Xia, and M.Y. Zheng, Effect of nano-precipitation on thermal conductivity and mechanical properties of Mg–2Mn–xLa alloys during hot extrusion, *J. Alloys Compd.*, 830(2020), art. No. 154570.

[14] C.Y. Su, D.J. Li, A.A. Luo, T. Ying, and X.Q. Zeng, Effect of solute atoms and second phases on the thermal conductivity of Mg–RE alloys: A quantitative study, *J. Alloys Compd.*, 747(2018), p. 431.

[15] W.L. Xiao, M.A. Easton, S.M. Zhu, M.S. Dargusch, M.A. Gibson, S.S. Jia, and J.F. Nie, Casting defects and mechanical properties of high pressure die cast Mg–Zn–Al–RE alloys, *Adv. Eng. Mater.*, 14(2012), No. 1-2, p. 68.

[16] L.F. Hou, Y.H. Wei, Y.G. Li, B.S. Liu, H.Y. Du, and C.L. Guo, Erosion process analysis of die-casting inserts for magnesium alloy components, *Eng. Fail. Anal.*, 33(2013), p. 457.

[17] X. Tian, L.M. Wang, J.L. Wang, Y.B. Liu, J. An, and Z.Y. Cao, The microstructure and mechanical properties of Mg–3Al–3RE alloys, *J. Alloys Compd.*, 465(2008), No. 1-2, p. 412.

[18] L.A. Dobrzański, T. Tański, L. Čížek, and Z. Brytan, Structure and properties of magnesium cast alloys, *J. Mater. Process. Technol.*, 192-193(2007), p. 567.

[19] A.A. Luo, Recent magnesium alloy development for automotive powertrain applications, *Mater. Sci. Forum*, 419-422(2003), p. 57.

[20] G.Y. Yuan, G.Q. You, S.L. Bai, and W. Guo, Effects of heat treatment on the thermal properties of AZ91D magnesium alloys in different casting processes, *J. Alloys Compd.*, 766(2018), p. 410.

[21] I.A. Anyanwu, Y. Gokan, S. Nozawa, A. Suzuki, S. Kamado, Y. Kojima, S. Takeda, and T. Ishida, Development of new die-castable Mg–Zn–Al–Ca–RE alloys for high temperature applications, *Mater. Trans.*, 44(2003), No. 4, p. 562.

[22] W.L. Xiao, S.S. Jia, L.D. Wang, Y.M. Wu, and L.M. Wang, The microstructures and mechanical properties of cast Mg–Zn–Al–RE alloys, *J. Alloys Compd.*, 480(2009), No. 2, p. L33.

[23] F. Shi, C.Q. Wang, and X.F. Guo, Microstructures and properties of as-cast $Mg_{92}Zn_4Y_4$ and $Mg_{92}Zn_4Y_3Gd_1$ alloys with LPSO phase, *Rare Met. Mater. Eng.*, 44(2015), No. 7, p. 1617.

[24] W.L. Xiao, M.A. Easton, M.S. Dargusch, S.M. Zhu, and M.A. Gibson, The influence of Zn additions on the microstructure and creep resistance of high pressure die cast magnesium alloy AE44, *Mater. Sci. Eng. A*, 539(2012), p. 177.

[25] V.D. Belov, A.V. Koltygin, N.A. Belov, and I.V. Plisetskaya, Innovations in cast magnesium alloys, *Metallurgist*, 54(2010), No. 5-6, p. 317.

[26] Z.R. Zeng, Y.M. Zhu, M.Z. Bian, S.W. Xu, C.H.J. Davies, N. Birbilis, and J.F. Nie, Annealing strengthening in a dilute Mg–Zn–Ca sheet alloy, *Scripta Mater.*, 107(2015), p. 127.

[27] M. Mabuchi and K. Higashi, Strengthening mechanisms of Mg–Si alloys, *Acta Mater.*, 44(1996), No. 11, p. 4611.

[28] T. Homma, S. Hirawatari, H. Sunohara, and S. Kamado, Room and elevated temperature mechanical properties in the as-extruded Mg–Al–Ca–Mn alloys, *Mater. Sci. Eng. A*, 539(2012), p. 163.

[29] S.M. Zhu, T.B. Abbott, M.A. Gibson, J.F. Nie, and M.A. Easton, Age hardening in die-cast Mg–Al–RE alloys due to minor Mn additions, *Mater. Sci. Eng. A*, 656(2016), p. 34.

[30] F. Wang, W.L. Xiao, M.W. Liu, J. Chen, X. Li, J.B. Xi, and C.L. Ma, Effects of alloying composition on the microstructures and mechanical properties of Mg–Al–Zn–Ca–RE magnesium alloy, *Vacuum*, 159(2019), p. 400.

[31] W.L. Xiao, S.S. Jia, J. Wang, J.L. Wang, and L.M. Wang, Investigation on the microstructure and mechanical properties of a cast Mg–6Zn–5Al–4RE alloy, *J. Alloys Compd.*, 458(2008), No. 1-2, p. 178.

[32] W.Q. Zhang, W.L. Xiao, F. Wang, and C.L. Ma, Development of heat resistant Mg–Zn–Al-based magnesium alloys by addition of La and Ca: Microstructure and tensile properties, *J. Alloys Compd.*, 684(2016), p. 8.

[33] A.K. Dahle, Y.C. Lee, M.D. Nave, P.L. Schaffer, and D.H. StJohn, Development of the as-cast microstructure in magnesium-aluminium alloys, *J. Light. Met.*, 1(2001), No. 1, p. 61.

[34] B.R. Tao, R.S. Qiu, Y.F. Zhao, Y.S. Liu, X.N. Tan, B.F. Luan, and Q. Liu, Effects of alloying elements (Sn, Cr and Cu) on second phase particles in Zr–Sn–Nb–Fe–(Cr, Cu) alloys, *J. Alloys Compd.*, 748(2018), p. 745.

[35] T. Wang, Research on the thermal conductivity of SiC/Al composite, *J. Synth. Cryst.*, 46(2017), No. 10, p. 2062.

[36] C.M. Wang, Y.G. Chen, S.F. Xiao, W.C. Ding, and X. Liu, Thermal conductivity and mechanical properties of as-cast Mg–3Zn–(0.5~3.5)Sn alloys, *Rare Met. Mater. Eng.*, 42(2013), No. 10, p. 2019.

[37] R.X. Zheng, J.P. Du, S. Gao, H. Somekawa, S. Ogata, and N. Tsuji, Transition of dominant deformation mode in bulk polycrystalline pure Mg by ultra-grain refinement down to sub-micrometer, *Acta Mater.*, 198(2020), p. 35.

[38] Z. Zhang, J.H. Zhang, J. Wang, Z.H. Li, J.S. Xie, S.J. Liu, K. Guan, and R.Z. Wu, Toward the development of Mg alloys with simultaneously improved strength and ductility by refining grain size via the deformation process, *Int. J. Miner. Metall. Mater.*, 28(2021), No. 1, p. 30.

[39] N. Ono, R. Nowak, and S. Miura, Effect of deformation temperature on Hall-Petch relationship registered for polycrystalline magnesium, *Mater. Lett.*, 58(2004), No. 1-2, p. 39.

[40] H. Somekawa and T. Mukai, Hall-Petch relation for deformation twinning in solid solution magnesium alloys, *Mater. Sci. Eng. A*, 561(2013), p. 378.

[41] F. Wang, T. Hu, Y.T. Zhang, W.L. Xiao, and C.L. Ma, Effects of Al and Zn contents on the microstructure and mechanical properties of Mg–Al–Zn–Ca magnesium alloys, *Mater. Sci. Eng. A*, 704(2017), p. 57.

[42] S.F. Liu, B. Li, X.H. Wang, W. Su, and H. Han, Refinement effect of cerium, calcium and strontium in AZ91 magnesium alloy, *J. Mater. Process. Technol.*, 209(2009), No. 8, p. 3999.

[43] F. Kabirian and R. Mahmudi, Effects of rare earth element additions on the impression creep behavior of AZ91 magnesium alloy, *Metall. Mater. Trans. A*, 40(2009), No. 9, p. 2190.

[44] B. Kondori and R. Mahmudi, Effect of Ca additions on the microstructure, thermal stability and mechanical properties of a cast AM60 magnesium alloy, *Mater. Sci. Eng. A*, 527(2010), No. 7-8, p. 2014.

[45] A.A. Luo and A.K. Sachdev, Development of a new wrought magnesium–aluminum–manganese alloy AM30, *Metall. Mater. Trans. A*, 38(2007), No. 6, p. 1184.

[46] Ø. Ryen, B. Holmedal, O. Nijs, E. Nes, E. Sjölander, and H.E. Ekström, Strengthening mechanisms in solid solution aluminum alloys, *Metall. Mater. Trans. A*, 37(2006), No. 6, p. 1999.